Experimental and theoretical investigation of enhancing the photocatalytic activity of Mg doped ZnO for nitrophenol degradation

Karim Tanji[1] · Imane El Mrabet[2] · Youssef Fahoul[1] · Ahmed Soussi[3] ·
Mohamed Belghiti[4] · Ilyass Jellal[5] · Yassine Naciri[6] · Abdelali El Gaidoumi[7] ·
Abdelhak Kherbeche[1]

Abstract

Magnesium-doped ZnO nanoparticles ($Mg_{0.1}Zn_{0.9}O$) were successfully synthesized following the solution combustion method. The effect of magnesium on the morphology, crystalline phases, and optical properties of the ZnO nanoparticles was studied. A relative band gap enhancement has been observed using the density functional theory (DFT) calculation through Mg doping from 3.19 eV to 3.24 eV. The photocatalytic degradation of 4-nitrophenol (4-NPh) has been investigated under UV irradiation in aqueous suspension where 1.5 g of $Mg_{0.1}Zn_{0.9}O/L$ removed 81% of 4-NPh (60 mg/L) under a pH solution of 12 within 120 min.

Graphical abstract
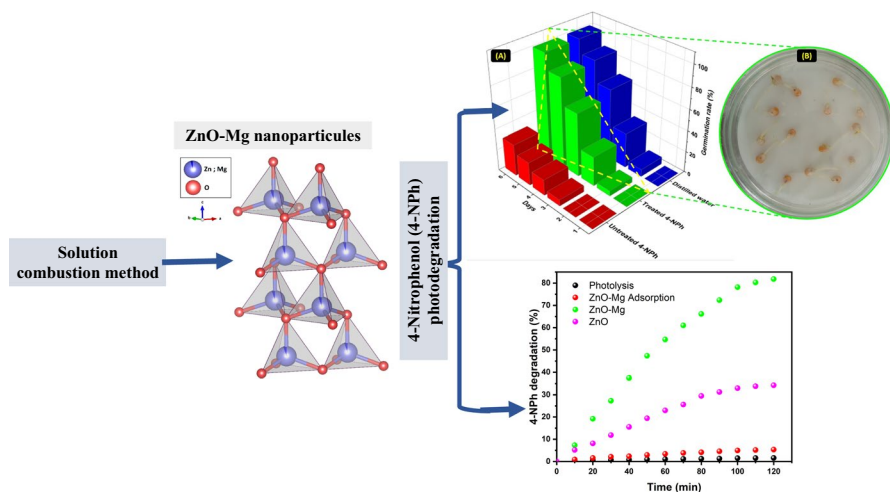
Extended author information available on the last page of the article

Introduction

Industrial water effluents represent a major drawback for the development of humanity, as they are potential causes of human health threats and aquatic life disturbance [1–3]. Since they are released in large quantities by various sources, toxic organic molecules make up a significant portion of industrial water effluents which are a great concern for the environment [4–7].

For instance, the charged wastewater with different organic molecules released into the environment can stop oxygen from dissolving and sunshine from penetrating, both of which are necessary for aquatic life [8–11]. Therefore, the purification of effluents is imperative before releasing them into receiving environments.

Nitrophenols are aromatic compounds, consisting of a benzene ring substituted by a hydroxyl (phenol) group as well as one or more nitro groups, although the term is most often used for mono-nitrate compounds. Nitrophenols are used as intermediates in the chemical, pharmaceutical, and armament industries. Hence, they are released into the environment through agriculture and wastewater discharge and the concentration that could be discharged is limited by USEPA at 0.01–2.0 μgL^{-1} [12].

Para-nitrophenol or 4-nitrophenol (4-NPh) is one of the most used phenolic compounds in large applications as raw materials or synthetic intermediates for dyes, drugs, pesticides, leather preservatives production, etc. [13]. The United States Environmental Protection Agency (USEPA) has classified 4-NPh in the first category of toxic substances because it is less soluble and stable in water and it accumulates in the food chain [14, 15].

The literature has reported many methods for the removal of organic molecules from real or model effluents. For instance, the conventional methods, including adsorption, coagulation-flocculation, and biological processes, all lead to a secondary residue that needs to be eventually managed. On the contrary, the new advanced oxidation processes (AOP), namely the photocatalysis process, show their effectiveness in the decomposition of harmful organic molecules into harmless products like CO_2 and H_2O [16–22]. These processes are based on the production of highly oxidizing species, mainly hydroxyl radicals (˙OH), which initiate a series of reactions that decomposes toxic molecules into inoffensive substances [8, 23, 24].

The scientific community has made great efforts to specifically customize and quickly adjust the characteristics of promising materials like zinc oxide (ZnO) due to its attractive photocatalytic activity. Despite having several benefits: high excitation binding energy (60 meV), excellent electrical, mechanical, and optical properties, simplicity in morphological control, relatively low cost, and non-toxicity, ZnO's photocatalytic activity is hindered by the high rate of recombination of photogenerated charge carriers, which limits the degradation reactions [25–27]. Metal doping is one of the most popular methods to increase the photocatalytic

efficiency of ZnO. Indeed, introducing metal ions into its matrix leads to the creation of defects that modify the properties (structural, optical, morphological, electrical…) of the material which improves its photocatalytic activity [28, 29].

Magnesium is a prime example of the wide variety of metals employed for bulk modifications of ZnO. Indeed, Mg modification can significantly enhance the photocatalytic performance of ZnO by producing Zn or oxygen vacancies since Mg has an approximately identical ionic radius to that of Zn and a small lattice mismatch of MgO with ZnO [30, 31]. Furthermore, Mg^{2+} has a higher ionization potential than Zn^{2+}, which means that it requires more energy to remove an electron from an Mg^{2+} ion. This can affect the material's ability to generate charge carriers upon light absorption, which can impact its photocatalytic activity [32].

The present work investigated the synthesis and characterization of Magnesium doped ZnO using the combustion method. Then it studied the factors influencing the photodegradation efficiency of 4-nitrophenol under UV light: the pH solution, the initial concentration of 4-NPh, and the catalyst amount. In addition, this work aimed to compare theoretical and experimental results in terms of electronic properties to investigate their effect on the photocatalytic process performance.

Experimental methods

Synthesis of samples

Comparing the combustion synthesis to conventional synthesis methods, it presents a potential alternative for obtaining a wide range of materials with various physical properties (refractory, optical, electronic, magnetic, catalytic …) [33, 34]. First, this process starts with the preparation of a gel formed by the evaporation of the mixture solution of zinc nitrate hexahydrate ($Zn(NO_3)_2 \cdot 6H_2O$), cobalt nitrate hexahydrate ($Mg(NO_3)_2 \cdot 6H_2O$) and urea (NH_2CONH_2) in distilled water using a magnetic stirrer at 150 °C until the total evaporation of water. Then the gel is placed in the oven for 30 min at 500 °C. Finally, the obtained catalyst $Zn_{0.9}Mg_{0.1}O$ is ground after cooling at room temperature.

The synthesis of $Mg_{0.1}Zn_{0.9}O$ is conducted following the stochiometric reaction (Eq. 1):

$$Zn\,(NO3)_2 6H_2O + Mg(NO_3)2H_2O + CH_4N_2O \rightarrow Mg_{0.1}Zn_{0.9}O \qquad (1)$$
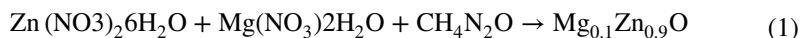
The final catalyst $Zn_{0.9}Mg_{0.1}O$ is denoted ZnO–Mg in the current work.

Experimental conditions for photocatalytic runs

The photocatalytic activity of the synthesized ZnO–Mg was assessed for 4-NPh degradation under UV light. Batch tests were performed by preparing 100 mL of 4-NPh solution, then 0.1 g of $Mg_{0.1}Zn_{0.9}O$ photocatalyst was added to the solution. The adsorption–desorption equilibrium was first ensured by keeping the mixture of the catalyst and 4-NPh solution in dark for 1 h before starting the photocatalytic

degradation test. Then, samples were collected each 10 min after irradiation with UV light, then suspended particles were removed by filtration for residual concentration measurement. The concentration of 4-NPh was determined using spectrophotometry technique at its maximum absorbance wavelength ($\lambda = 340$ nm) by a UV–Visible spectrophotometer (J.P.SELECTA, S.A.VR-2000) with a 1 cm path length spectrometric quartz cell.

The effect of the catalyst mass (0.5; 1; 1.5 g L^{-1}), pH (2; 4; 6; 8; 10; 12), and concentration of 4-NPh (20; 40; 60 mg L^{-1}) on the photodegradation yield was investigated. To calculate the degradation of 4-nitrophenol, Eq. 2 was used:

$$\text{Degradation \%} = \frac{c_o - c_t}{c_o} \times 100 \tag{2}$$

Here C_0 and C_t are the concentrations of 4-NPh before and after the photocatalysis test, respectively.

All experiments were conducted in a cylindrical photoreactor made of stainless steel. Its schematic representation is illustrated in Fig. S1 *(See the supplementary file)*. To reach the solution saturation with oxygen, the air was bubbled by an air pump. To ensure the homogeneity of the catalyst particles in the solution, it was stirred at 300 rpm. To have homogeneous radiation during the experiments, the reactor was equipped with four UV lamps which emit mainly at 365 nm (15W, Philips).

Characterization techniques

$Mg_{0.1}Zn_{0.9}O$ nanoparticles were characterized by X-ray diffraction (XRD) using a diffractometer (X'PERT PRO from Panalytical) with Cu K$_\alpha$ radiation at 30 kV and 450 W in the range of $2\theta = 5°–80°$. To calculate the Brunauer–Emmett–Teller surface area (S_{BET}) the nitrogen (N_2) adsorption/desorption method was used (Micromeritics ASAP2420). To examine the catalysts' morphology, scanning electron microscopy (SEM) coupled with Energy Dispersed Spectroscopy (EDS) and transmission electron microscopy (TEM-STEM) were used. The UV–visible spectrophotometer equipped with an integrating sphere (PerkinElmer Lambda 1050) using $BaSO_4$ as a reference was used to obtain the UV diffuse reflectance spectra (DRS) in the range 200–800 nm.

Computational methods

The first principle calculations were conducted using the full-potential linearized augmented-plane wave (FP-LAPW) method based on the density of state (DFT) in the WIEN2K software package [35]. The Tran-Blaha modified Becke-Johnson exchange potential (TB-mBJ) approximation, was developed to investigate the exchange–correlation effect. The self-consistent calculations are used to be converged when the total energy of the system is set within 10^{-5} Ry. The wave functions cut-off magnitude was set at $R_{MT} \times K_{max} = 9$, in the interstitial spaces, where R_{MT} represents the lowest atomic muffin-tin sphere radius and K_{max} represents the largest K vector in the plane wave extension. The cutoff energy was set at -6.0

Ry. The valence wave functions inside the muffin-tin spheres were expanded up to $l_{max} = 10$, while the charge density was Fourier expanded up to $G_{max} = 12$ (a.u.)$^{-1}$. About 700 k-points based on a $3 \times 2 \times 1$ Monkhorst–Pack (MP) are used in the first Brillouin [36].

Results and discussions

Characterization of the photocatalyst

X-ray diffraction patterns

To study the impact of magnesium on zinc oxide lattice and to identify the crystal structures of pristine ZnO and ZnO–Mg, XRD analysis was carried out. Fig. 1A reveals the presence of high intensity peaks, suggesting the good crystallinity of the
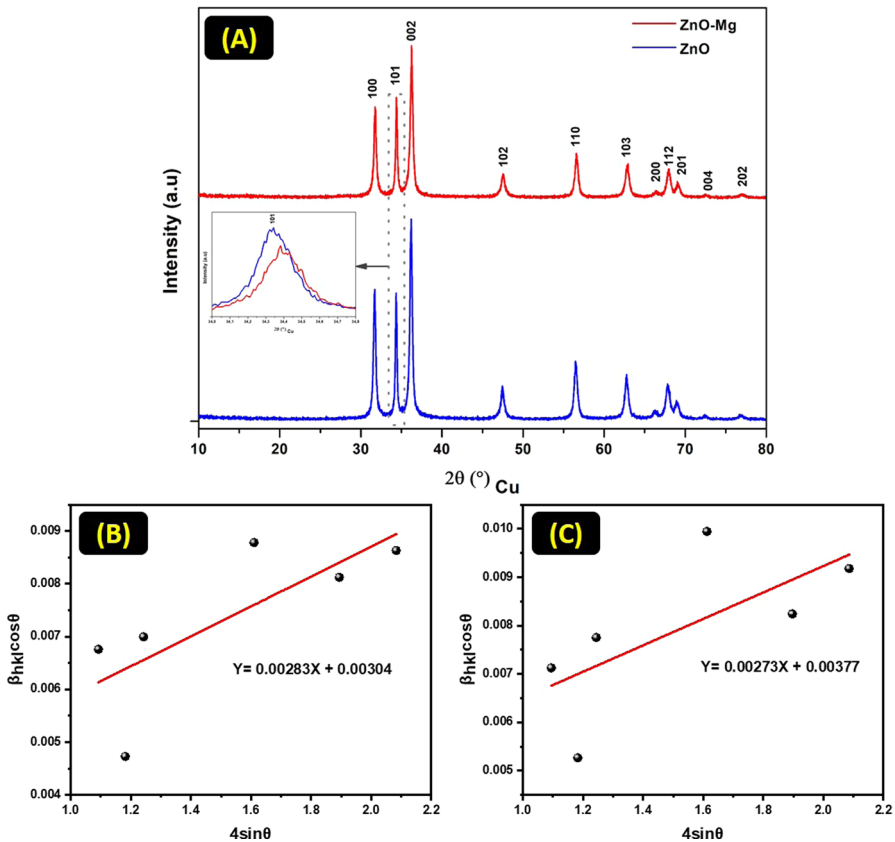

Fig. 1 **A** The XRD analysis of pristine ZnO (blue curve) and ZnO doped with Mg (red curve). The inset shows a magnification between the angles 2Θ 34° and 34.8°, **B** the plot for $4\sin\theta$ versus $\beta_{hkl} \cos\theta$ of ZnO, and **C** the plot for $4\sin\theta$ versus $\beta_{hkl} \cos\theta$ of ZnO–Mg. (Color figure online)

two synthesized materials. In addition, all peaks are perfectly indexed to the crystal structure of wurtzite-type ZnO according to JCPDS N° 36-1451. It is also noticed a similarity between the blue and red curves of the two materials ZnO and ZnO doped with Mg, respectively, with the absence of Mg peaks for the doped product. The inset in the figure represents a magnification between the angles 2Ɵ 34° and 34.8°. Moreover, a very slight shifting of the peaks of the doped material compared to the pure ZnO material is remarked, proving then a modification in the crystal lattice due to the replacement of Zn by Mg. This hypothesis was consolidated by increasing the lattice parameters of the Mg-doped product.

Table 1 contains the parameters a, b, and c, the volume of the lattice, as well as the crystallite size, estimated from the Williamson–Hall formula (Eq. 3).

$$\beta_{hkl} \cos\theta = \frac{k\lambda}{D} + 4\,\varepsilon \sin\theta \qquad (3)$$

Here λ is the X-ray wavelength, β the observed peaks' full-width-at-half-maximum, θ the incident angle and ε is the anisotropic strain.

Fig. 1B and C illustrate $4\sin\theta$ versus $\beta_{hkl}\cos\theta$ which was used to estimate the crystallite size of the prepared samples from the linear fit of data (Eq. 3).

Fig. S2 shows a 3D visualization of the ZnO crystal structure depicted using the structural analysis software VESTA. The experimental structure of ZnO can be described as a series of plans, with each Zn^{2+} being surrounded by an alternately positioned tetrahedra of oxygen atoms along the c-axis.

Diffuse reflectance spectra

The optical properties of pure ZnO and ZnO–Mg nanoparticles were studied by diffuse reflection. Fig. 2 shows the UV–vis spectra of both materials, where a broad and intense absorption at about 386 nm is detected. The decrease in optical absorbance may be due to various factors such as defects in grain structure, particle size, and lack of oxygen. Moreover, extrapolating the plot of the Kubelka–Munk $(\alpha h\nu)^n = k(h\nu - E_g)$ curve to zero results in the determination of the band gap energy. Where n is the frequency of the incident radiation, E_g is the band gap energy, α is the sample optical absorbance, and $h\nu$ is the photon energy. As presented in the inset of Fig. 2, the band gaps are estimated to be 3.24 and 3.31 eV which corresponds to ZnO pristine and ZnO–Mg, respectively. This relative increase of E_g confirms the modification of the crystal lattice of ZnO by Mg.

Table 1 Retiveled affinment and crystallite size

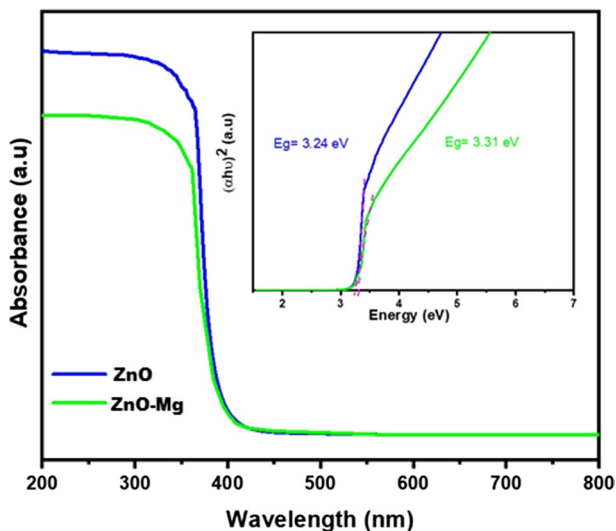| Photocatalyst	$a=b$ (Å)	c (Å)	c/a	V (Å³)	Crystallite size (nm)
ZnO	3.2534 (3)	5.2126 (5)	1.6022	47.784 (8)	45
ZnO/Mg	3.2501 (2)	5.2089 (4)	1.6026	47.652 (7)	36

Fig. 2 UV–visible DRS and the plot of $(\alpha h\nu)^2$ versus $h\nu$ of ZnO–Mg

XPS investigations

To investigate the oxidation state and elemental composition of the synthesized ZnO–Mg, Casa software was used for the deconvolution and overlapping of the peaks based on the Gaussian fitting. Fig. S3 indicates the presence of O (1 s), Zn (2p), and Mg (2p) characteristic peaks. The peaks of C(1 s) (292 and 287.3 eV) were used as a calibration reference. On the hand, the peaks O(1 s) look symmetrical with a binding energy of 531.6 and 530.2 eV attributed to the lattice oxygen of the prepared sample ZnO–Mg. The peaks of Zn 2p3/2 and Zn 2p1/2 at 1022.4 and 1045.5 eV refer to the presence of Zn^{2+} in ZnO–Mg. Besides, the spin energy separation between them which is equal to 22.6 proves the presence of Zn species in the sample at the Zn^{2+} chemical state. The Mg 2p symmetric peak at 51.7 eV indicates the existence of Mg atoms in the MgO state and its position at 49.8 eV can be attributed to the existence of Mg^{2+} replacing Zn^{2+}.

Morphology and elemental composition

The effect of Mg doping on the morphology of the final product was examined by SEM analysis. Fig. S4 shows the micrographs of ZnO–Mg with different magnifications. It is noticed that the material is composed of an aggregation of nanometric spheres with high homogeneity. The ZnO–Mg particles' nanometric size is expected to be advantageous for photocatalytic activity.

TEM analysis

To further explore the morphology, crystallinity, and chemical composition of the ZnO–Mg sample, TEM measurements coupled with EDX analysis were carried out. The TEM images of ZnO–Mg NPs as well as the elemental mappings shown in Fig. S5 indicate the spherical tendency of ZnO–Mg nanoparticles. The elemental mapping shows the good dispersion of Zn and Mg, proving consequently the successful synthesis of ZnO doped with Mg.

Surface area analysis

Several factors related to the semiconductor could influence photocatalytic efficiency, including morphology, specific surface, defects, and surface hydroxyl groups [37, 38]. The Barett–Joyner–Halenda method was used to measure the specific surfaces and the distribution of pores in ZnO and Mg-doped ZnO to further assess the mechanism of photocatalytic degradation (Fig. 4S). According to the Brunauer–Deming–Deming–Teller classification, the N_2 adsorption–desorption isotherms are type III for both materials [39]. A type H3 hysteresis loop can be observed at P/P_0 values between 0.9 and 1, revealing the existence of mesoporous in ZnO and ZnO doped with Mg.

The pore size distributions of ZnO–Mg and pure ZnO are shown in the insets of Figs. S6SA and S6B. The ZnO sample has both large and smaller mesopores with pore sizes of 25 and 3.0 nm, respectively. While the ZnO–Mg sample has larger mesopores with a pore peak centered at 65 nm and smaller ones with a pore peak centered at 2.5 nm. The hollow interiors of the ZnO microspheres are connected to the bigger mesopores. While the smaller mesopores illustrate the field between the nanospheres. The ZnO-Mg particles were found to have a higher specific surface area of 10.36 m^2/g while this of ZnO is 7.77 m^2/g, which can promote better photodegradation compared to pure ZnO.

Photocatalytic activity under UV light

It is well known that the efficiency of photocatalytic degradation of 4-NPh is influenced by different parameters such as pH, catalyst amount, and solution concentration. To examine the effect of pH, the photocatalyst mass was fixed at 1 g/L, and a series of 60 mg/L of 4-NPh solution were prepared, with different pH from 2 to 12 (Fig. S7). Fig. S7A displays the results of the effect of the initial pH solution of 4-NPh on the degradation efficiency using ZnO–Mg. The variation of the photocatalytic activity as a function of the pH shows that the efficiency of the degradation goes from 30 to 78% by increasing the pH from 2 to 12. Moreover, the pH of the point of zero charge (pH_{pzc}) of ZnO has been found to be around 8.7 (Fig. S7D). At pH levels below to pH_{pzc} value, the presence of free electrons from the N and O atoms of 4-NPh molecules and the positive surplus charges on the catalyst

surface (caused by the particular adsorption of H^+) enhance the migration of toxic molecules to the catalyst's surface. As a result, more acidic pH levels are preferred for the optimum photodegradation responses.

The effect of the initial 4-NPh concentration on the photocatalytic activity of Mg-doped ZnO was assessed as well. Indeed, the concentration of 4-NPh is varied between 20 and 60 mg/L under the conditions: 1 g/L of ZnO-Mg catalyst, pH = 5.08, and temperature of 25 ± 4 °C. According to Fig. S7B, the increase of 4-NPh concentration resulted in an enhancement of the photocatalytic activity. The concentration increases of 4-NPh from 20 to 40 mg/L led to an increase of 4-NPh degradation from 52 to 60% and achieved 75% of 4-NPh degradation for a concentration of 60 mg/L. As the 4-NPh concentration rises, additional pollutants are attracted to the catalyst surface, where they are to interact with hydroxyl radicals. In this instance, the 4-NPh molecules possibly have directly reacted with hydroxyl radicals with a nanosecond lifetime.

Fig. S7C shows the effect of the photocatalyst mass on the degradation of 4-NPh. The photocatalyst mass was varied from 0.5 g/L to 1.5 g/L and other parameters were fixed ([4-NPh] = 60 mg/L, pH = 5.08, T = 25 ± 4 °C). The increase in the catalyst amount has enhanced the photocatalytic efficiency which reached its highest value at 1.5 g/L with a yield of 76%. As the catalyst concentration increases, more active ZnO-Mg sites are available to absorb photons and produce electron/hole pairs, and therefore the photodegradation rate increases.

Fig. 3 presents the photocatalytic activity efficiency of ZnO and Mg-doped ZnO under UV light irradiation and optimum parameters. To test the stability of 4-NPh, a solution of 4-NPh was exposed to UV light without photocatalyst addition (photolysis). The results indicated that the concentration of 4-NPh remained constant, suggesting that the 4-NPh is stable under UV light irradiation. The adsorption
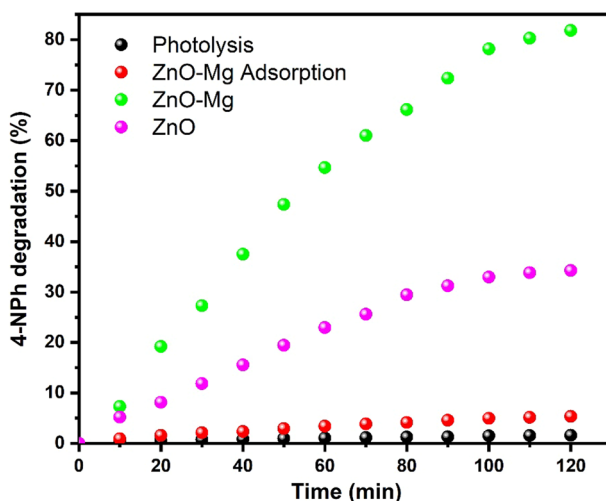

Fig. 3 Adsorption and photodegradation tests of 4-NPh using ZnO-Mg under UV light illumination and optimum parameters (catalyst mass = 1.5 g/L, 4-NPh concentration = 60 mg/L and pH = 12)

capacity of the catalyst was studied before starting the photocatalytic degrading process. The results showed that Mg-doped ZnO has a poor adsorption capacity that does not exceed 6% in 120 min. Thereafter, ZnO alone provided a low photocatalytic activity for 4-NPh degradation under UV light illumination and reached 35% of 4-NPh (60 mg/L) during 120 min. On the contrary, Mg-doped ZnO showed an enhancement of photocatalytic activity under UV light that reached 81% of 4-NPh (60 mg/L) in 120 min. Hence, the Mg-doped ZnO presented a higher photocatalytic efficiency ($+47\%$) compared to ZnO alone. The enhancement of the photocatalytic activity with Mg doping is probably due to the increase in the specific surface and the reduction of photogenerated charges recombination. Some results were found by Etacheri et al., where the photocatalytic activity of ZnO was improved with Mg doping, which could be due to the enhanced textural properties and efficient electron–hole separation [40, 41].

To provide further insights into the 4-NPh photodegradation using ZnO–Mg, radical and hole scavengers' experiments were carried out by investigating the degradation efficiency with and without the presence of the catalyst or the scavenger. For this purpose, silver nitrate (SN), chloroform (Chl), tert-butanol (t-ButOH), and Ethylene diamine tetra-acetic acid (EDTA-2Na) were used as scavengers of e^-, $O_2^{\cdot-}$, $OH^\cdot$ and h^+, respectively [42]. All the experiments were conducted under the same conditions with the addition of the appropriate scavenger. The results are presented in Fig. 4A indicate that the addition of SN and EDTA-2Na does not influence much the photodegradation efficiency of 4-NPh, whereas, the addition of t-ButOH and Chl significantly decreases its photodegradation, which indicates that the hydroxyl and superoxide radicals are the main reactive species involved in the photodegradation process of 4-NPh using ZnO–Mg.

Fig. 4B illustrates the results of the recycling tests of the Mg-doped ZnO photocatalyst used for the photodegradation of a 4-NPh solution under UV radiation for 120 min. The photodegradation rate of 4-NPh using ZnO–Mg photocatalyst
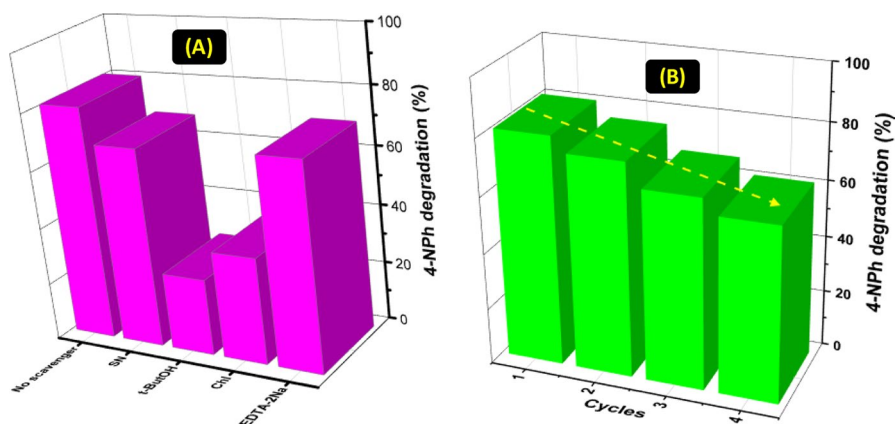

Fig. 4 **A** Influence of active species scavengers on 4-NPh degradation and **B** 4-NPh conversion percentages during 4 consecutive cycles over ZnO–Mg (catalyst mass = 1.5 g/L, [4-NPh] = 60 mg/L, pH = 12, T = 25 °C ± 4 °C, contact time = 120 min)

showed a slight decrease after each cycle, indicating that ZnO–Mg retains its stability after four cycles of photocatalytic tests.

To assess the toxicity of 4-NPh before and after degradation, the corn kernels were chosen to study their germination. Thus, corn kernels were put in three solutions with the same volume: (i) distilled water, (ii) untreated 4-NPh solution (60 mg/L), and (iii) treated 4-NPh solution (60 mg/L) using ZnO–Mg photocatalyst. The germination rate of corn kernels in untreated 4-NPh solution, treated 4-NPh solution, and distilled water are shown in Fig. 5A. Due to the toxicity of the solution, the inhibitory effect has a direct impact on the number of germinated grains. The germination in distilled water solution was pretty standard after 6 days and reached 100%, as expected. However, the germination was only 30% on the sixth day in the untreated 4-NPh solution, demonstrating that the high toxicity of this solution prevents corn kernels from germinating. On the sixth day, the germination rate of corn kernels in the 4-NPh solution treated with the ZnO-Mg photocatalyst reached 87% and the image illustrated in Fig. 5B shows the majority of seeds are germinated. This outcome demonstrates that following the photodegradation test by the ZnO–Mg photocatalyst, the toxicity of the 4-NPh solution was highly reduced.

After investigating the effect of the key parameters on the photodegradation of 4-NPh and studying the kinetic, scavenging, reuse, and germination tests, the mechanism that might have occurred was proposed (Fig. S8). Indeed, when ZnO–Mg is exposed to UV irradiation, the photons will excite electrons and then will move from the valence band (VB) to the conduction band (CB) which will create electron–hole pairs. Whenever the separation of electrons from the catalyst is efficient and the mitigation of charge carrier recombination is low, the photocatalytic activity
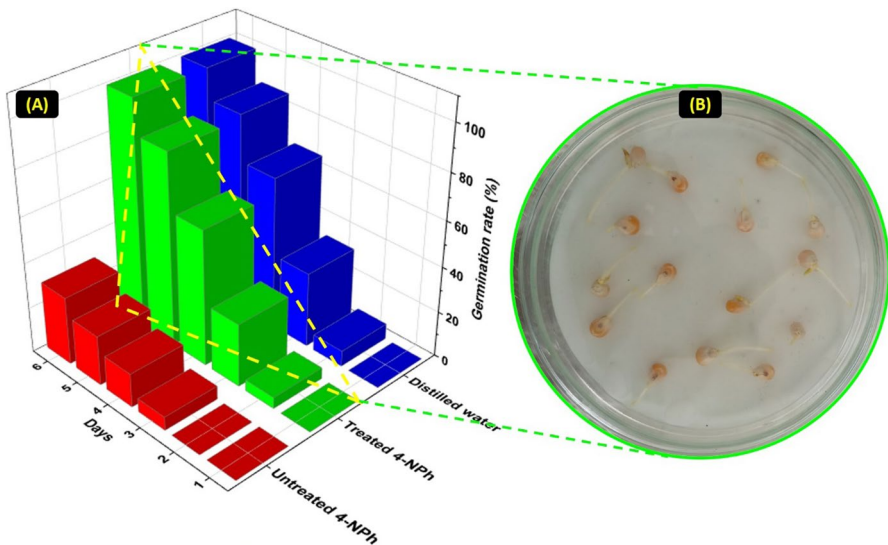

Fig. 5 **A** Germination rate (%) of corn kernels in treated 4-NPh solution, untreated 4-NPh solution and distilled water during 6 days; **B** Image of corn kernels immersed in treated 4-NPh solution (after 6 days, T = 25 °C ± 4 °C)

is higher. Holes will react with hydroxyl molecules to generate hydroxyl radicals (OH·), while electrons with oxygen produce superoxide radicals (O_2·⁻), both OH· and O_2·⁻ will react with 4-NPh to decompose it to CO_2 and H_2O [43].

Electronic structure properties

Fig. 6A, B illustrates the band structure of pure ZnO and Mg-doped ZnO (MZO). Thus, the calculated band gap of pure ZnO and MZO is 3.19 eV and 3.24 eV, respectively. It is practically the same as the experimental value (3.18 eV) [44]. This discrepancy has little effect on the analysis of the relative values of the electronic structures and optical properties of pure ZnO and MZO films.

The valence band for pure ZnO is from −5.52 to 0 eV and the conduction band starts at 3.19 eV. As seen in Fig. 6, the CB and VB shift toward the lower energy regions for the doped ZnO. For the pure ZnO, the conduction band minimum (CBM) and valence band maximum (VBM) lie at the Γ, implying a direct bandgap of 3.19 eV which is in good agreement with the experimental optical bandgap.

As a comparison, the density of states (DOS) of ZnO and MZO is also calculated in Fig. 7 A and B. In the case of the pure ZnO, the VB region is formed by the Zn:3d states and a small contribution from the O_2 state, and the conduction band consists mainly of the O:2p states. For MZO films, the VB region is formed by the O:2p and Zn:3d states and a small contribution of Manganese states particularly Mg:3 s, the CB consists mainly of the O:2p states and a small proportion of Zn:3d. For pure ZnO, the number of down-spin electrons is the same as the number of up-spin electrons while the spin polarization phenomenon was not observed. On other hand, due to the difference between the number of both spins as shown in Fig. 7B, the spin polarization in both bands is observed for MZO. It is noticed that the band structure of MZO shows a metallic behavior with the majority-spin and the minority-spin bands being metallic. This provides a half-metallic (HM) gap, which is an important parameter to determine the application in spintronic devices.
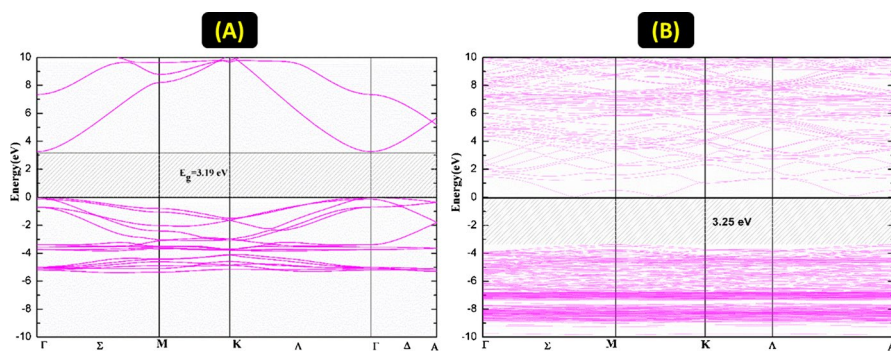

Fig. 6 The band structures along high-symmetry lines within the first Brillouin zone of ZnO and ZnO/Mg with TB-mBJ approximation
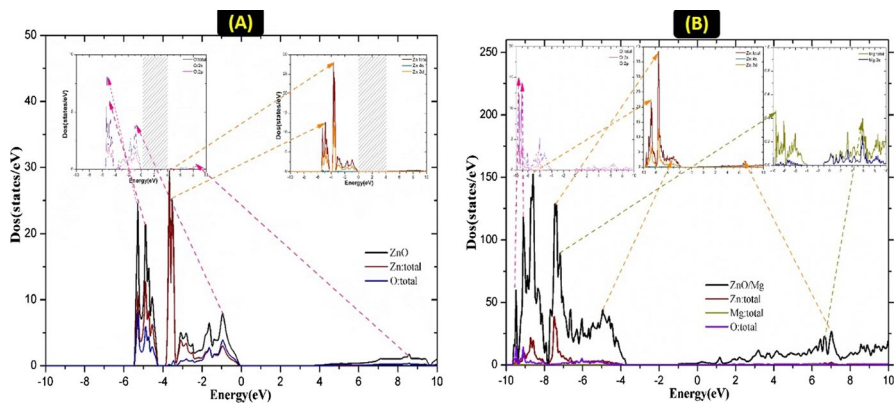
Fig. 7 The densities of states of ZnO and ZnO/Mg with TB-mBJ approximation

Comparison with the literature

By reviewing the literature, it is found that many articles have dealt with the photodegradation of 4-NPh in an aqueous solution [45–56]. Table 2 presents a comparative study of the photodegradation efficiency under UV light of 4-Nph using several photocatalysts. The prepared ZnO-Mg exhibits a remarkable degradation rate (75%) of 4-Nph, considering the removal time (120 min) and the initial concentration of the pollutant (60 mg/L) compared to the photocatalysts cited in the literature. Moreover, the significant difference in the reported efficiencies may be due to the variation of synthesis methods, doping agents, light nature, catalyst mass, solution pH, and the initial concentrations of 4-NPh.

Conclusion

In the present work, photocatalytic degradation of 4-NPh has been studied using various semiconductor metal oxide catalysts. The impact of Mg doping on ZnO electronic properties was assessed using first-principles calculations based on density functional theory and compared with those of pure ZnO. The results indicated that 4-NPh was successfully degraded by $Mg_{0.1}Zn_{0.9}O$ photocatalyst in an aqueous solution under UV irradiation. Furthermore, it was confirmed that the catalyst mass, the initial concentration of 4-NPh, and the pH solution obviously affected the degradation efficiency of $Mg_{0.1}Zn_{0.9}O$. Indeed, the photocatalytic efficiency has increased with the increase of catalyst mass while it decreased with the increase of the initial concentration of 4-NPh. Hence, 81% of 4-NPh (60 mg/L) was removed using 1.5 g of $Mg_{0.1}Zn_{0.9}O$/L within 120 min under pH solution 12. These findings are of great interest and contribution to the photocatalysis field and the development of advanced processes for wastewater purification.

Table 2 Comparison of various catalysts efficiency towards 4-NPh photodegradation

Catalyst (Mass)	4-Nitrophenol concentration	Light source	Efficiency/Time	References
Mg doped ZnO (1.5 g/L)	60 mg/L	UV light (2 × 15 W UV lamp)	81%/120 min	This Study
Ag/ZnO (0.66 g/L)	10 mg/L	UV-C (30 W lamp)	52%/90 min	[45]
ZrO$_2$-Cr$_2$O$_3$ (0.01 g/L)	10 mg/L	UV light	80.6%/100 min	[46]
ZnO (1 g/L)	10 mg/L	UV light (30 W Hg lamp)	14%/195 min	[49]
La/ZnO (1 g/L)	10 mg/L	UV light (30 W Hg lamp)	78%/195 min	[49]
Nd/ZnO (1 g/L)	10 mg/L	UV light (30 W Hg lamp)	83%/195 min	[49]
Sm/ZnO (1 g/L)	10 mg/L	UV light (30 W Hg lamp)	53%/195 min	[49]
TiO$_2$ (1 g/L)	10 mg/L	UV light (150 W Hg lamp)	18%/120 min	[50]
Graphene modified TiO$_2$ (1 g/L)	10 mg/L	UV light (150 W Hg lamp)	59.5%/120 min	[50]
SrTiO$_3$ (0.4 g/L)	10 mg/L	UV light (125 W medium pressure Hg vapor lamp)	55%/150 min	[51]
TiO$_2$ (0.4 g/L)	10 mg/L	UV light (125 W medium pressure Hg vapor lamp)	62%/150 min	[51]
SrTiO$_3$/TiO$_2$ (0.4 g/L)	10 mg/L	UV light (125 W medium pressure Hg vapor lamp)	99%/150 min	[51]
TiO$_2$ (1 g/L)	1 mg/L	UV light (125-W Hg lamp)	45%/180 min	[52]
B/TiO$_2$ (1 g/L)	1 mg/L	UV light (125-W Hg lamp)	70%/180 min	[52]
TiO$_2$ (0.5 g/L)	4 mg/L	UV light (20 W Hg lamp)	83%/60 min	[53]
TiO$_2$ (1 g/L)	5 mg/L	UV light (160 W high-pressure Hg lamp)	40%/120 min	[54]
TiO$_2$/Kaolinite (1 g/L)	10 mg/L	UV light (20 W UV lamp)	90%/240 min	[55]
TiO$_2$/Halloysite (1 g/L)	10 mg/L	UV light (12 W UV lamp)	70%/240 min	[56]
TiO$_2$/Rectorite (1 g/L)	10 mg/L	UV light (20 W UV lamp)	70%/240 min	[47]
TiO$_2$/Sepiolite (1.5 g/L)	10 mg/L	UV light (20 W UV lamp)	79%/240 min	[48]

Declarations

Conflict of interest The authors declare that they have no known competing financial interests or personal relationships that could have appeared to influence the work reported in this paper.

References

1. Benkhaya S, M'rabet S, El Harfi A (2020) A review on classifications, recent synthesis and applications of textile dyes. Inorg Chem Commun 115:107891. https://doi.org/10.1016/J.INOCHE.2020.107891
2. Gonçalves IMC, Gomes A, Brás R et al (2000) Biological treatment of effluent containing textile dyes. Color Technol 116:393–397. https://doi.org/10.1111/j.1478-4408.2000.tb00016.x
3. Chequer FMD, de Oliveira GAR, Ferraz ERA et al (2013) Textile dyes: dyeing process and environmental impact. Eco-Friendly Text Dye Finish. https://doi.org/10.5772/53659
4. El Hajam M, Kandri NI, Plavan GI et al (2020) Pb2+ ions adsorption onto raw and chemically activated dibetou sawdust: application of experimental designs. J King Saud Univ—Sci 32:2176–2189. https://doi.org/10.1016/J.JKSUS.2020.02.027
5. El Hajam M, Idrissi Kandri N, Harrach A et al (2019) Adsorption of Methylene Blue on industrial softwood waste "Cedar" and hardwood waste "Mahogany": comparative study. Mater Today Proc 13:812–821. https://doi.org/10.1016/J.MATPR.2019.04.044
6. Gita S, Hussan A, Choudhury TG (2017) Impact of textile dyes waste on aquatic environments and its treatment. Environ Ecol 35:2349–2353
7. Dra A, Tanji K, Arrahli A et al (2020) Valorization of oued sebou natural sediments (Fez-Morocco area) as adsorbent of methylene blue dye : kinetic and thermodynamic study. Sci World J 2020:2187129. https://doi.org/10.1155/2020/2187129
8. Ghosh Ray S, Ghangrekar MM (2018) Comprehensive review on treatment of high-strength distillery wastewater in advanced physico-chemical and biological degradation pathways. Int J Environ Sci Technol 161(16):527–546. https://doi.org/10.1007/S13762-018-1786-8
9. Thiam A, Tanji K, Assila O et al (2020) Valorization of date pits as an effective biosorbent for remazol brilliant blue adsorption from aqueous solution. J Chem 2020:14. https://doi.org/10.1155/2020/4173152
10. Puvaneswari N, Muthukrishnan J, Gunasekaran P (2006) Toxicity assessment and microbial degradation of azo dyes. Indian J Exp Biol 44:618–626
11. Ejder-Korucu M, Gürses A, Dogar Ç et al (2015) Removal of organic dyes from industrial effluents: an overview of physical and biotechnological applications. Green Chem Dye Remov Waste Water Res Trends Appl. https://doi.org/10.1002/9781118721001.CH1

12. Balakrishnan A, Gaware GJ, Chinthala M (2023) Heterojunction photocatalysts for the removal of nitrophenol: a systematic review. Chemosphere 310:136853. https://doi.org/10.1016/J.CHEMOSPHERE.2022.136853

13. Xiong Z, Zhang H, Zhang W et al (2019) Removal of nitrophenols and their derivatives by chemical redox: a review. Chem Eng J 359:13–31. https://doi.org/10.1016/J.CEJ.2018.11.111

14. Raza W, Lee J, Raza N et al (2019) Removal of phenolic compounds from industrial waste water based on membrane-based technologies. J Ind Eng Chem 71:1–18. https://doi.org/10.1016/J.JIEC.2018.11.024

15. Bilal M, Bagheri AR, Bhatt P, Chen S (2021) Environmental occurrence, toxicity concerns, and remediation of recalcitrant nitroaromatic compounds. J Environ Manag 291:1685. https://doi.org/10.1016/J.JENVMAN.2021.112685

16. Djaballah AM, Bagtache R, Tartaya S, Trari M (2021) Synthesis and characterization of the semiconductor $CuBi_2O_4$ for optical and dielectric studies. Application to methyl violet degradation under visible light. React Kinet Mech Catal 134:1055–1067. https://doi.org/10.1007/S11144-021-02115-4/FIGURES/12

17. Bagtache R, Brahimi R, Abdmeziem K, Trari M (2021) Preparation and photo-electrochemical characterization of KAlPO4F: application to photodegradation of methyl violet under sunlight. React Kinet Mech Catal 133:1111–1120. https://doi.org/10.1007/S11144-021-02010-Y/FIGURES/8

18. Djaballah AM, Bagtache R, Benlambarek M, Trari M (2022) Semiconducting properties of $CuBi_2O_4$ prepared at low temperature: application to oxygen evolution under visible light. React Kinet Mech Catal 135:2769–2781. https://doi.org/10.1007/S11144-022-02260-4/FIGURES/10

19. El Mrabet I, Ihssane B, Valdés H, Zaitan H (2022) Optimization of Fenton process operating conditions for the treatment of the landfill leachate of Fez city (Morocco). Int J Environ Sci Technol 19:3323–3336. https://doi.org/10.1007/s13762-021-03393-0

20. Majdoub A, El Mrabet I, Majdoub M et al (2022) In situ deposition of Ag nanoparticles onto PE/rGO hybrids for the dip-catalytic hydrogenation of 4-nitrophenol into 4-aminophenol. Int J Environ Anal Chem. https://doi.org/10.1080/03067319.2022.2089034

21. El Hajam M, Kandri NI, Zerouale A et al (2022) Lignocellulosic nanocrystals from sawmill waste as biotemplates for free-surfactant synthesis of photocatalytically active porous silica. ACS Appl Mater Interfaces 14:19547–19560. https://doi.org/10.1021/acsami.2c02550

22. Zouheir M, Assila O, Tanji K et al (2021) Bandgap optimization of sol-gel-derived TiO_2 and its effect on the photodegradation of formic acid. Nano Futur 5:025004

23. Fahoul Y, Zouheir M, Tanji K, Kherbeche A (2022) Synthesis of a novel ZnAl2O4/CuS nanocomposite and its characterization for photocatalytic degradation of acid red 1 under UV illumination. J Alloys Compd 889:161708. https://doi.org/10.1016/j.jallcom.2021.161708

24. Mahtab MS, Farooqi IH, Khursheed A (2022) Zero Fenton sludge discharge: a review on reuse approach during wastewater treatment by the advanced oxidation process. Int J Environ Sci Technol 19:2265–2278. https://doi.org/10.1007/S13762-020-03121-0/FIGURES/1

25. Belghiti M, Tanji K, El Mersly L et al (2022) Fast and non-selective photodegradation of basic yellow 28, malachite green, tetracycline, and sulfamethazine using a nanosized ZnO synthesized from zinc ore. React Kinet Mech Catal 135:2265–2278. https://doi.org/10.1007/s11144-022-02232-8

26. Tanji K, Navio JA, Martín-Gómez AN et al (2020) Role of Fe(III) in aqueous solution or deposited on ZnO surface in the photoassisted degradation of rhodamine B and caffeine. Chemosphere 241:125009. https://doi.org/10.1016/j.chemosphere.2019.125009

27. Tanji K, Zouheir M, Hachhach M et al (2021) Design and simulation of a photocatalysis reactor for rhodamine B degradation using cobalt-doped ZnO film. React Kinet Mech Catal 134:1017–1038. https://doi.org/10.1007/s11144-021-02116-3

28. Qi K, Yu J (2020) Modification of ZnO-based photocatalysts for enhanced photocatalytic activity. Interface Sci Technol 31:265–284. https://doi.org/10.1016/B978-0-08-102890-2.00008-7

29. Samadi M, Zirak M, Naseri A et al (2016) Recent progress on doped ZnO nanostructures for visible-light photocatalysis. Thin Solid Films 605:2–19. https://doi.org/10.1016/j.tsf.2015.12.064

30. Hamdy MS, Chandekar KV, Shkir M et al (2020) Novel Mg@ZnO nanoparticles synthesized by facile one-step combustion route for anti-microbial, cytotoxicity and photocatalysis applications. J Nanostructure Chem 11:147–163. https://doi.org/10.1007/s40097-020-00355-9

31. Zyoud AH, Zubi A, Zyoud SH et al (2019) Kaolin-supported ZnO nanoparticle catalysts in self-sensitized tetracycline photodegradation: zero-point charge and pH effects. Appl Clay Sci 182:1094. https://doi.org/10.1016/J.CLAY.2019.105294

32. Heo YW, Ivill MP, Ip K et al (2008) ZnO: growth, doping & processing. Mater Today 7:34–40. https://doi.org/10.1016/S1369-7021(04)00287-1

33. Patil KC, Aruna ST, Mimani T (2002) Combustion synthesis: an update. Curr Opin Solid State Mater Sci 6:507–512. https://doi.org/10.1016/S1359-0286(02)00123-7

34. Moore JJ, Feng HJ (1995) Combustion synthesis of advanced materials: part I. Reaction parameters. Prog Mater Sci 39:243–273. https://doi.org/10.1016/0079-6425(94)00011-5

35. Blaha P, Schwarz K, Madsen GKH, et al (2022) WIEN2K, an augmented plane wave plus local orbitals program for calculating crystal properties

36. Morgan WS, Jorgensen JJ, Hess BC, Hart GLW (2018) Efficiency of generalized regular k-point grids. Comput Mater Sci 153:424–430. https://doi.org/10.1016/j.commatsci.2018.06.031

37. Achouri F, Corbel S, Aboulaich A et al (2014) Aqueous synthesis and enhanced photocatalytic activity of ZnO/Fe_2O_3 heterostructures. J Phys Chem Solids 75:1081–1087. https://doi.org/10.1016/J.JPCS.2014.05.013

38. Moussa H, Girot E, Mozet K et al (2016) ZnO rods/reduced graphene oxide composites prepared via a solvothermal reaction for efficient sunlight-driven photocatalysis. Appl Catal B Environ 185:11–21. https://doi.org/10.1016/J.APCATB.2015.12.007

39. Sing KSW, Everett DH, Haul RAW et al (1985) Reporting physisorption data for gas/solid systems with special reference to the determination of surface area and porosity. Pure Appl Chem 57:603–619. https://doi.org/10.1351/pac198557040603

40. Etacheri V, Roshan R, Kumar V (2012) Mg-doped ZnO nanoparticles for efficient sunlight-driven photocatalysis. ACS Appl Mater Interfaces 4:2717–2725. https://doi.org/10.1021/AM300359H/SUPPL_FILE/AM300359H_SI_001.PDF

41. Zheng ALT, Abdullah CAC, Chung ELT, Andou Y (2022) Recent progress in visible light-doped ZnO photocatalyst for pollution control. Int J Environ Sci Technol. https://doi.org/10.1007/s13762-022-04354-x

42. Cen S, Lv X, Jiang Y et al (2020) Synthesis and structure of iron–copper/hollow magnetic/metal–organic framework/coordination sites in a heterogeneous catalyst for a Fenton-based reaction. Catal Sci Technol 10:6687–6693. https://doi.org/10.1039/D0CY01027H

43. Divband B, Jodaei A, Khatamian M (2019) Enhancement of photocatalytic degradation of 4-nitrophenol by integrating Ag nanoparticles with ZnO/HZSM-5 nanocomposite. Iran J Catal 9:63–70

44. Soussi A, Ait Hssi A, Boulkaddat L et al (2022) Structural, optical and electronic properties of La-doped ZnO thin films: experimental study and DFT calculations. Phys B Condens Matter 643:4181. https://doi.org/10.1016/J.PHYSB.2022.414181

45. Divband B, Khatamian M, Eslamian GRK, Darbandi M (2013) Synthesis of Ag/ZnO nanostructures by different methods and investigation of their photocatalytic efficiency for 4-nitrophenol degradation. Appl Surf Sci 284:80–86. https://doi.org/10.1016/J.APSUSC.2013.07.015

46. Noroozi Z, Ali Rasekh H, Jaafar Soltanianfard M (2019) Preparation and characterization of ZrO_2-Cr_2O_3 nanocomposite as a p-n heterojunction by a facile sol-gel method: a kinetic investigation on the removal of p-nitrophenol dye from aqueous media. Polyhedron 168:11–20. https://doi.org/10.1016/J.POLY.2019.04.033

47. Zhang Y, Guo Y, Zhang G, Gao Y (2011) Stable TiO2/rectorite: preparation, characterization and photocatalytic activity. Appl Clay Sci 51:335–340. https://doi.org/10.1016/J.CLAY.2010.12.023

48. Zhang Y, Wang D, Zhang G (2011) Photocatalytic degradation of organic contaminants by TiO2/sepiolite composites prepared at low temperature. Chem Eng J 173:1–10. https://doi.org/10.1016/J.CEJ.2010.11.028

49. Khatamian M, Khandar AA, Divband B et al (2012) Heterogeneous photocatalytic degradation of 4-nitrophenol in aqueous suspension by Ln (La^{3+}, Nd^{3+} or Sm^{3+}) doped ZnO nanoparticles. J Mol Catal A Chem 365:120–127. https://doi.org/10.1016/J.MOLCATA.2012.08.018

50. Liu X, Zhao L, Lai H et al (2017) Efficient photocatalytic degradation of 4-nitrophenol over graphene modified TiO_2. J Chem Technol Biotechnol 92:2417–2424. https://doi.org/10.1002/JCTB.5251

51. Devi LG, Anitha BG (2018) Exploration of vectorial charge transfer mechanism in TiO_2/$SrTiO_3$ composite under UV light illumination for the degradation of 4-nitrophenol: a comparative study with TiO2 and SrTiO3. Surf Interfaces 11:48–56. https://doi.org/10.1016/J.SURFIN.2018.02.005

52. Yadav V, Verma P, Sharma H et al (2020) Photodegradation of 4-nitrophenol over B-doped TiO_2 nanostructure: effect of dopant concentration, kinetics, and mechanism. Environ Sci Pollut Res 27:10966–10980. https://doi.org/10.1007/S11356-019-06674-X

53. Ilyas H, Qazi IA, Asgar W et al (2011) Photocatalytic degradation of nitro and chlorophenols using doped and undoped titanium dioxide nanoparticles. J Nanomater. https://doi.org/10.1155/2011/589185

54. Li SX, Zheng FY, Liu XL et al (2005) Photocatalytic degradation of p-nitrophenol on nanometer size titanium dioxide surface modified with 5-sulfosalicylic acid. Chemosphere 61:589–594. https://doi.org/10.1016/J.CHEMOSPHERE.2005.02.054

55. Zhang Y, Gan H, Zhang G (2011) A novel mixed-phase TiO$_2$/kaolinite composites and their photocatalytic activity for degradation of organic contaminants. Chem Eng J 172:936–943. https://doi.org/10.1016/J.CEJ.2011.07.005

56. Zheng P, Du Y, Chang PR, Ma X (2015) Amylose–halloysite–TiO$_2$ composites: Preparation, characterization and photodegradation. Appl Surf Sci 329:256–261. https://doi.org/10.1016/J.APSUSC.2014.12.158

Authors and Affiliations

Karim Tanji[1] · **Imane El Mrabet[2]** · **Youssef Fahoul[1]** · **Ahmed Soussi[3]** · **Mohamed Belghiti[4]** · **Ilyass Jellal[5]** · **Yassine Naciri[6]** · **Abdelali El Gaidoumi[7]** · **Abdelhak Kherbeche[1]**

✉ Karim Tanji
karim.tanji@usmba.ac.ma

[1] Laboratory of Catalysis, Process, Materials and Environment, Higher School of Technology, University Sidi Mohamed Ben Abdellah, Fez, Morocco

[2] Department of Physics-Chemistry, Polydisciplinary Faculty of Ouarzazate, University of Ibn Zohr, Agadir, Morocco

[3] Materials and Renewable Energy Laboratory, Ibn Zohr University, Agadir, Morocco

[4] Laboratoire des Nanomatériaux, l'énergie et l'environnement, Faculté des Sciences Semlalia, Université Cadi Ayyad, BP 2390, 40000 Marrakech, Morocco

[5] Laboratory of Materials Physics and Subatomics (LMPS), Department of Physics, Faculty of Sciences, Ibn Tofail University, BP 133, Kenitra, Morocco

[6] Laboratory of Materials and Environment, Faculty of Sciences, Ibn Zohr University, Agadir, Morocco

[7] École Supérieure de Technologie de Khénifra, Université Sultan Moulay Slimane, Beni Mellal, Morocco